Prepared for submission to JCAP

Backreaction of axion-SU(2) dynamics during inflation

Oksana Iarygina,[a,b] **Evangelos I. Sfakianakis,**[c,d] **Ramkishor Sharma,**[a,b] **and Axel Brandenburg**[a,e,f,g]

[a]Nordita, KTH Royal Institute of Technology and Stockholm University, Hannes Alfvéns väg 12, 10691 Stockholm, Sweden

[b]The Oskar Klein Centre, Department of Physics, Stockholm University, AlbaNova, 10691 Stockholm, Sweden

[c]Department of Physics, Case Western Reserve University, 10900 Euclid Avenue, Cleveland, OH 44106, USA

[d]Institut de Fisica d'Altes Energies (IFAE), The Barcelona Institute of Science and Technology (BIST), Campus UAB, 08193 Bellaterra, Barcelona, Spain

[e]The Oskar Klein Centre, Department of Astronomy, Stockholm University, 10691 Stockholm, Sweden

[f]McWilliams Center for Cosmology & Department of Physics, Carnegie Mellon University, Pittsburgh, PA 15213, USA

[g]School of Natural Sciences and Medicine, Ilia State University, 3-5 Cholokashvili Avenue, 0194 Tbilisi, Georgia

E-mail: oksana.iarygina@su.se, esfakianakis@ifae.es, ramkishor.sharma@su.se, brandenb@nordita.org

Abstract. We consider the effects of backreaction on axion-SU(2) dynamics during inflation. Accounting for the backreaction leads to a new late-time dynamical attractor solution for the axion field and the vacuum expectation value of the gauge field, where the latter has a sign-flipped value with respect to the chromo-natural inflation solution. Our findings are of particular interest to the phenomenology of axion-SU(2) inflation, significantly broadening the viable parameter space. In addition, the backreaction effects lead to characteristic oscillatory features in the primordial gravitational wave background, potentially detectable in upcoming observational experiments.[**OI**: add linear approximation, Hartree]

Contents

1 Introduction

Natural inflation was originally proposed in order to address the UV sensitivity problem of inflation [1, 2]. By identifying the inflaton with an axion, a pseudo-scalar field possessing a shift symmetry, the infinite series of higher-order terms in the potential are set to zero. The inflationary potential is generated through instanton effects and in the early versions of natural inflation the potential is a sinusoidal function of the field.

The shift symmetry also dictates the possible couplings of the inflaton to other fields. In particular, an axion can only couple derivatively to other fields. Furthermore, the lowest order coupling to fermions and gauge bosons are $\bar{\psi}\gamma_\mu\gamma^5\partial\mu\phi\psi$ and $\phi F\tilde{F}$, respectively, where $\tilde{F}$ is the dual field strength tensor.

The coupling of an axion inflaton to gauge fields through a Chern-Simons term has attracted significant attention in the literature. In the case of an Abelian field, the parity-violating nature of the coupling leads to the two helicities developing a different effective frequency. One of them can even become tachyonic, when the velocity of the inflaton is high enough. After the end of inflation, tachyonic production of gauge fields can lead to instantaneous preheating. Identifying the gauge field with the hypercharge sector of the Standard Model can lead to the generation of observationally relevant cosmological magnetic fields. During inflation, the production of gauge fields can lead to observable non-Gaussianity.

Depending on the axion-gauge coupling strength, the tachyonic amplification of the gauge fields can arise during inflation. In this case, the generation of gauge fields leads to a significant backreaction on the inflaton, leading to a sudden drop of its velocity. Once the gauge fields are diluted by the expansion of space-time, the backreaction term subsides and

the inflaton starts rolling again. This can lead to periodic bursts of gauge field production during inflation [3–6], as has been shown analytically and numerically. However, recent lattice simulations showed that the inclusion of inhomogeneous backreaction and a larger dynamical range can significantly change the resulting dynamics [7].

Despite the interesting backreaction dynamics that occurs for large axion-gauge coupling, the rolling of the axion is in the linear regime determined by the potential and Hubble friction. By replacing the Abelian field with a non-Abelian one, this ceases to be true. The fact that SU(2) fields (see ref. [8] for the generalization to SU(N) fields) possess a non-trivial vacuum structure leads to a new inflationary attractor, in which the dominant source of friction for the rolling axion is not the Hubble term, but the non-Abelian field VEV [9–12].

This family of models, collectively named chromo-natural inflation, allows for slow-roll inflation even in steep potentials. Due to the parity-violating Chern-Simons coupling, one of the tensor modes of the SU(2) sector experiences a similar instability to one of the helicities in the Abelian case. However, the fact that the SU(2) tensor mode is linearly coupled to the gravitational sector leads to a similar enhancement of chiral gravitational waves.

While chromo-natural inflation with a cosine potential has been shown to be incompatible with CMB observations [9], spontaneous breaking of the SU(2) symmetry brings the model in agreement with current data [13]. A further generalization of CNI was proposed in ref. [14], where the axion-SU(2) action was treated as a spectator sector. This separates the inflationary sector, which is responsible for scalar fluctuations, from the chromo-natural sector, which can produce detectable B-modes, while remaining subdominant in both scalar fluctuations and energy density during inflation. This family of models can be described as "spectator chromo-natural inflation" (SCNI) and their GW spectra are directly related to the shape of the axion potential [15].

In this work, we go beyond previous studies of axion-SU(2) dynamics during inflation by considering the effects of backreaction. We use the linear equations of motion for the tensor SU(2) fluctuations and self-consistently solve the background equations for the axion and SU(2) VEV, including the homogeneous (averaged) backreaction from tensor fluctuations. This is in spirit similar to the analysis performed in ref. [3] for the Abelian case. We must note that ref. [6] largely validated these calculations, while more recent simulations [7] point out the importance of inhomogeneous effects during the strong backreaction regime. Our analysis can therefore be considered an important and necessary first step into the uncharted mild backreaction regime of axion-SU(2) dynamics during inflation.

Our manuscript is organized as follows. In section 2 we review spectator chromo-natural inflation and provide the necessary equations and analytical solutions. The numerical procedure is described in section 3, followed by the results and semi-analytical analysis of the solution. We conclude in Section 4.

2 Review of spectator axion-SU(2) inflation

In this section, we review the spectator axion-SU(2) inflation or the spectator chromo-natural inflation model, outlining the background and perturbation analysis based on previous works [9, 11, 14].

2.1 Model and background evolution

The action for spectator axion-SU(2) inflation is given by [14]

$$S = \int d^4x\sqrt{-\det(g_{\mu\nu})}\left[\frac{M_{\rm Pl}^2}{2}R - \frac{1}{2}(\partial\phi)^2 - V(\phi) - \frac{1}{2}(\partial\chi)^2 - U(\chi) - \frac{1}{4}F^a_{\mu\nu}F^{a\,\mu\nu} + \frac{\lambda\chi}{4f}F^a_{\mu\nu}\tilde{F}^{a\,\mu\nu}\right], \tag{2.1}$$

where R is the space-time Ricci scalar, $\phi(t)$ and $V(\phi)$ are the inflaton field and its potential, respectively, $\chi(t)$ and $U(\chi)$ are the axion field and its potential, $F^a_{\mu\nu} = \partial_\mu A^a_\nu - \partial_\nu A^a_\mu - g\epsilon^{abc}A^b_\mu A^c_\nu$ is the field strength of the SU(2) gauge field A^a_μ, $\tilde{F}^{a\,\mu\nu} = \epsilon^{\mu\nu\rho\sigma}F^a_{\rho\sigma}/\left(2\sqrt{-\det g_{\mu\nu}}\right)$ is its dual ($\epsilon^{\mu\nu\alpha\beta}$ is the antisymmetric tensor and $\epsilon^{0123} = 1$), g is the gauge field coupling, λ is the coupling constant between the gauge and axion sectors, and f is the axion decay constant.

In this work we use the axion potential of the form

$$U(\chi) = \mu^4\left(1 + \cos\frac{\chi}{f}\right), \tag{2.2}$$

where μ is a constant that sets the energy scale of the axion field. In this convention, the axion field takes values $\chi \in [0, \pi f]$. The potential for the inflation field, $V(\phi)$, is left unspecified.

We work with the FLRW metric

$$ds^2 = -dt^2 + a(t)^2\delta_{ij}dx^i dx^j, \tag{2.3}$$

where i, j indicate the spatial directions. An isotropic solution for the background is given by the gauge field configuration

$$A^a_0 = 0, \quad A^a_i = \delta^a_i a(t)Q(t), \tag{2.4}$$

which is also an attractor [16]. For this ansatz, the closed system of equations for the vacuum expectation value (VEV) of the gauge field $Q(t)$ and the Hubble parameter $H(t)$ is given by

$$M_{\rm Pl}^2\dot{H} = -\frac{1}{2}\dot{\phi}^2 - \frac{1}{2}\dot{\chi}^2 - \left[(\dot{Q} + HQ)^2 + g^2Q^4\right], \tag{2.5}$$

$$3M_{\rm Pl}^2H^2 = \frac{\dot{\phi}^2}{2} + V(\phi) + \frac{\dot{\chi}^2}{2} + U(\chi) + \frac{3}{2}\left(\dot{Q} + HQ\right)^2 + \frac{3}{2}g^2Q^4, \tag{2.6}$$

$$\ddot{Q} + 3H\dot{Q} + \left(\dot{H} + 2H^2\right)Q + 2g^2Q^3 = \frac{g\lambda}{f}\dot{\chi}Q^2, \tag{2.7}$$

$$\ddot{\chi} + 3H\dot{\chi} + U_\chi(\chi) = -\frac{3g\lambda}{f}Q^2\left(\dot{Q} + HQ\right), \tag{2.8}$$

$$\ddot{\phi} + 3H\dot{\phi} + V_\phi(\phi) = 0, \tag{2.9}$$

where $V_\phi(\phi) = \partial V(\phi)/\partial\phi$, $V_\chi(\chi) = \partial U(\chi)/\partial\chi$, and an overdot denotes a derivative with respect to cosmic time t. The Hubble slow-roll parameters are defined as

$$\epsilon_H = -\frac{\dot{H}}{H^2}, \quad \eta_H = -\frac{\ddot{H}}{2H\dot{H}}, \tag{2.10}$$

which are much smaller than unity during inflation. The first slow-roll parameter ϵ_H contains contributions from the inflaton field ϕ and the spectator sector that consists of the axion and gauge fields

$$\epsilon_H = \epsilon_\phi + \epsilon_{Q_E} + \epsilon_{Q_B} + \epsilon_\chi. \tag{2.11}$$

The various contributions are defined as

$$\epsilon_\phi = \frac{\dot{\phi}^2}{2M_{\rm Pl}^2 H^2}, \quad \epsilon_{Q_E} = \frac{(\dot{Q}+HQ)^2}{M_{\rm Pl}^2 H^2}, \quad \epsilon_{Q_B} = \frac{g^2 Q^4}{M_{\rm Pl}^2 H^2}, \quad \epsilon_\chi = \frac{\dot{\chi}^2}{2M_{\rm Pl}^2 H^2}. \tag{2.12}$$

For the axion-gauge sector to remain a spectator, their energy densities must be subdominant to that of the inflaton, i.e.,

$$\rho_\phi \gg \rho_\chi,\, \rho_{Q_E},\, \rho_{Q_B}, \tag{2.13}$$

where the energy densities are given by

$$\rho_\phi = \frac{1}{2}\dot{\phi}^2 + V(\phi), \quad \rho_\chi = \frac{1}{2}\dot{\chi}^2 + U(\chi), \quad \rho_{Q_E} = \frac{3}{2}(\dot{Q}+HQ)^2, \quad \rho_{Q_B} = \frac{3}{2}g^2Q^4. \tag{2.14}$$

The original chromo-natural inflation model in the slow-roll approximation has an attractor solution [9, 11]

$$\begin{aligned} \frac{\lambda}{f}\dot{\chi} &= 2gQ + \frac{2H^2}{gQ}, \\ \dot{Q} &= -HQ + \frac{f}{3g\lambda}\frac{U_\chi}{Q^2}. \end{aligned} \tag{2.15}$$

The VEV of the gauge field that minimizes the axion effective potential is

$$Q \simeq \left(\frac{-fU_\chi(\chi)}{3g\lambda H}\right)^{1/3}, \tag{2.16}$$

which is a solution of Eq. (2.15) when Q is small. It is convenient to introduce the parameters

$$m_Q = \frac{gQ}{H}, \quad \xi = \frac{\lambda}{2fH}\dot{\chi}, \tag{2.17}$$

where the dimensionless mass parameter m_Q characterizes the mass of the gauge field fluctuations and controls their amplification. On the chromo-natural inflation attractor, m_Q and ξ are related via $\xi \simeq m_Q + 1/m_Q$.

2.2 Perturbations

Let us now review the perturbations in the spectator axion-SU(2) model. We adopt the gauge choice and decomposition for field fluctuations following ref. [17] of the form

$$\begin{aligned} \phi &= \phi + \delta\phi, \\ \chi &= \chi + \delta\chi, \\ A^1_\mu &= a\,(Y_1,\, Q+\delta Q + t_+,\, t_\times,\, \partial_z M_1), \\ A^2_\mu &= a\,(Y_2,\, t_\times,\, Q+\delta Q - t_+,\, \partial_z M_2), \\ A^3_\mu &= a\,(Y_z,\, 0,\, 0,\, Q+\delta Q + \partial_z\partial_z M), \end{aligned} \tag{2.18}$$

together with

$$g_{\mu\nu} = a^2 \begin{pmatrix} -1+2\varphi & B_1 & B_2 & \partial_z B \\ & 1+h_+ & h_\times & 0 \\ & & 1-h_+ & 0 \\ & & & 1 \end{pmatrix}. \tag{2.19}$$

The perturbations consist of seven scalar modes ($\delta\phi$, $\delta\chi$, Y, δQ, M, φ, B), six vector modes ($Y_{1,2}$, $M_{1,2}$, $B_{1,2}$) and four tensor modes (t_+, $t_\times$, h_+, $h_\times$). At the linear level, all perturbations are decoupled from each other. Vector perturbations decay on super-horizon scales and at the linear level metric fluctuations can be neglected [17].

The scalar perturbations have been studied in detail at the linear (add more citations) and nonlinear levels [18]. It was shown that for $m_Q < \sqrt{2}$, the scalar perturbations are tachyonically unstable [17]. The combination from linear and nonlinear analyses leads to the constraint [18]

$$\sqrt{2} < m_Q \leq \left(\frac{g^2}{32\pi^2\, P_{\zeta,\mathrm{CMB}}}\right)^{1/4} \simeq 35\sqrt{g}, \tag{2.20}$$

on the parameter m_Q, where $P_{\zeta,\mathrm{CMB}} = 2.1 \cdot 10^{-9}$.

Let us now turn to the discussion of tensor perturbations. It is convenient to express the plus and cross polarizations of tensor perturbations via the left-handed and right-handed polarizations as

$$h_+ = \frac{h_L + h_R}{\sqrt{2}}, \quad h_\times = \frac{h_L - h_R}{i\sqrt{2}}, \quad t_+ = \frac{t_L + t_R}{\sqrt{2}}, \quad t_\times = \frac{t_L - t_R}{i\sqrt{2}}. \tag{2.21}$$

We canonically normalize them by introducing

$$h_{L,R} = \frac{\sqrt{2}}{M_p a}\psi_{L,R}, \quad t_{L,R} = \frac{1}{\sqrt{2}a}T_{L,R}. \tag{2.22}$$

We will work with conformal time defined as

$$\eta = \int_0^t \frac{dt}{a(t)}, \tag{2.23}$$

which, with the near de Sitter expansion, leads to

$$a = -\frac{1}{H\eta} \tag{2.24}$$

for the scale factor. In the following, derivatives with respect to η are denoted by primes. In conformal time and to leading order in slow-roll, the equations of motion for the tensor perturbations are

$$\psi''_{R,L} + \left(k^2 - \frac{2}{\eta^2}\right)\psi_{R,L} = \frac{2\sqrt{\epsilon_{Q_E}}}{\eta}T'_{R,L} + \frac{2\sqrt{\epsilon_{Q_B}}}{\eta^2}(m_Q \pm k\eta)T_{R,L}, \tag{2.25}$$

$$T''_{R,L} + \left\{k^2 + \frac{2}{\eta^2}\left[m_Q\xi \pm k\eta(m_Q + \xi)\right]\right\}T_{R,L} = -\frac{2\sqrt{\epsilon_{Q_E}}}{\eta}\psi'_{R,L} + \frac{2}{\eta^2}\left[\sqrt{\epsilon_{Q_B}}(m_Q \pm k\eta) + \sqrt{\epsilon_{Q_E}}\right]\psi_{R,L}. \tag{2.26}$$

Here k is the wave number. The spectator axion-SU(2) model is known to have a transient growth of one of the polarizations of the gauge field tensor modes that leads to the production of chiral gravitational waves (GW). The produced GW background is enhanced with respect to the standard single-field slow-roll models of inflation with predicted amplitudes potentially observable by near-future B-mode experiments.

The total GW power spectrum is defined as

$$\sum_{i,j}\langle h_{ij}(\vec{k})h_{ij}(\vec{k'})\rangle = (2\pi)^3\delta^3(\vec{k}+\vec{k'})\,\mathcal{P}_h^{\rm tot}(k), \tag{2.27}$$

where $\mathcal{P}_h^{\rm tot}(k)$ can be expressed in terms of left and right polarization modes as

$$\mathcal{P}_h^{\rm tot}(k) = 2\mathcal{P}_h^L(k) + 2\mathcal{P}_h^R(k), \tag{2.28}$$

where $\mathcal{P}_h^{(s)}$ is the late-time sourced GW power spectrum, defined as

$$\mathcal{P}_h^{(s)}(k) = \frac{H^2}{\pi^2 M_{\rm Pl}^2}\left|\sqrt{2k}\left(-\frac{k}{aH}\right)\lim_{\eta\to 0}\psi_R^{(s)}(k,\eta)\right|^2. \tag{2.29}$$

It is convenient to introduce a parameter that characterizes the enhancement of the GW background with respect to the vacuum prediction,

$$\mathcal{R}_{\rm GW} = \frac{\mathcal{P}_h^{(s)}}{\mathcal{P}_h^{(v)}}, \tag{2.30}$$

where the vacuum prediction for the power spectrum is given by

$$\mathcal{P}_h^{(v)}(k) = \frac{2H^2}{\pi^2 M_{\rm Pl}^2}. \tag{2.31}$$

In order to have sizable GW production, the parameter range of the model has to be chosen such that $\mathcal{R}_{\rm GW} \gtrsim 1$. This requirement leads to the constraint [18]

$$g \lesssim 1.8\cdot 10^{-5}\, m_Q^2\, e^{1.8 m_Q}. \tag{2.32}$$

The growth of tensor modes results in the backreaction [14, 18, 19] on the background equations of motion (2.5)–(2.9). Taking into account the contribution from backreaction, the background equations of motion in conformal time take the form

$$Q'' + 2\mathcal{H}Q' + \left(\mathcal{H}' + \mathcal{H}^2\right)Q + 2g^2a^2Q^3 - \frac{g\lambda}{f}a\chi' Q^2 + a^2\mathcal{T}_{\rm BR}^Q = 0, \tag{2.33}$$

$$\chi'' + 2\mathcal{H}\chi' + a^2U_\chi(\chi) + \frac{3g\lambda}{f}aQ^2\left(Q' + \mathcal{H}Q\right) + a^2\mathcal{T}_{\rm BR}^\chi = 0, \tag{2.34}$$

with $\mathcal{H} = a'/a$ and

$$\mathcal{T}_{\rm BR}^Q = \frac{g}{3a^2}\int\frac{d^3k}{(2\pi)^3}\left(\xi H - \frac{k}{a}\right)|T_R|^2, \tag{2.35}$$

$$\mathcal{T}_{\rm BR}^\chi = -\frac{\lambda}{2a^4 f}\frac{d}{d\eta}\int\frac{d^3k}{(2\pi)^3}\left(a\, m_Q H - k\right)|T_R|^2. \tag{2.36}$$

It is worth noting that in this work we consider *homogeneous* backreaction, where the spatial gradients of inflation and axion fields are neglected, keeping these fields homogeneous during inflation.

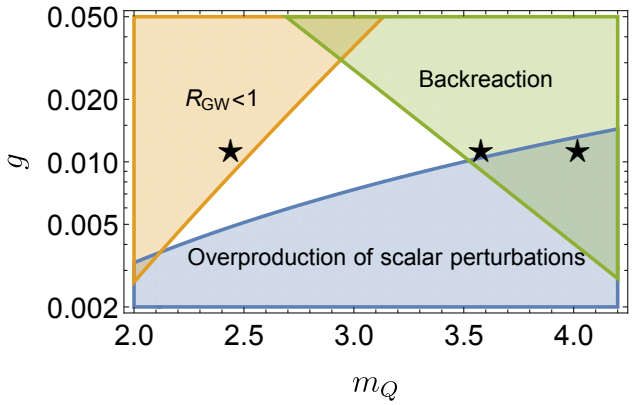

Figure 1. Constraints on the spectator axion-SU(2) model similar as in ref. [18] with indication of parameters used in the current work. The stars correspond to the parameters (from left to right) $m_Q = 2.44$, 3.58, 4.19 with $g = 0.011$ (runs μ_1, μ_4, μ_5 from Table 1.)

In the small-backreaction regime with an approximately constant m_Q parameter, the spectator axion-SU(2) model can be solved analytically [10]. The regime of small backreaction is achieved with the constraint [18]

$$g \ll \left(\frac{24\pi^2}{2.3 \cdot e^{3.9 m_Q}} \frac{1}{1 + m_Q^{-2}} \right)^{1/2} . \tag{2.37}$$

In figure 1, we plot the three constraints (2.20), (2.32), and (2.37) on the parameter range of the theory, indicating the fiducial parameters used in the current work.

3 Numerical treatment of the backreaction

To study the backreaction in axion-SU(2) inflation, we now solve the perturbation equations along with those for the background numerically. We begin by describing the numerical method and then discuss the results.

3.1 Numerical implementation

We solve Equations (2.25) and (2.26) for both the left- and right-handed components of $T_{R,L}$ and $\psi_{R,L}$. For each perturbation variable, we solve the equations for the real and imaginary parts and represent them on a k mesh to compute the integrals in (2.35) and (2.36). For most of our studies, we use the logarithmic wave number along with conformal time as the independent coordinates. In that case, we use n_k points in $\ln k$ that are separated by uniform intervals in $\ln k$ in the range

$$n_{\min} \leq \ln(k/a_0 H) \leq n_{\max}. \tag{3.1}$$

To solve the background (2.33) and (2.34), we compute the integrals (2.35) and (2.36) up to second-order accuracy. We advance the solution in conformal time using a third-order time-stepping scheme. The initial conformal time is η_i and the final one is η_f. In practice, we choose $\eta_i = -\mathcal{H}_i^{-1}$ with $\mathcal{H}_i = a_i H$ and $a_i = 1$ along with $\eta_f = -10^{-5}$, which corresponds to a total duration of $N \approx 25$ e-folds. The length of the conformal time step is then usually chosen to be $\Delta\eta = 10^{-6}/\mathcal{H}$.

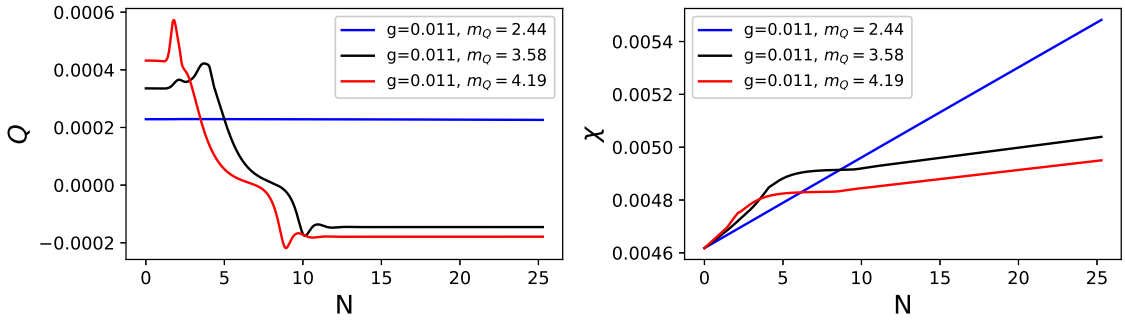

Figure 2. Evolution of Q and χ with N is shown for different initial parameters. The red, black, and blue curves correspond to runs $\mu1$, $\mu4$, and $\mu5$ respectively from table 1 with $g = 0.011$ and $m_Q = 2.44$, 3.58, 4.19 (from left to right). For the blue curve, the backreaction is negligible therefore the value of Q remains constant. However, for a larger value of m_Q (black and red curve), the backreaction effects are important. [**OI**: can we do solid, dotted and dashed plot styles for curves as in fig.3?]

It is convenient to use the compute and data management infrastructure provided by the Pencil Code [20], which allows for efficient parallelization using the Message Passing Interface library. In some exploratory cases, we also solved the equations on a mesh where $n_{\rm min}$ and $n_{\rm max}$ grow in time such that the main contributions to the integral are captured during the entire evolution.

We initialize the perturbation variables with the Bunch-Davies initial condition. Specifically, we set the initial conditions for the real and imaginary parts of the perturbation variables as follows:

$$T_{R,L} = \frac{e^{-ik\eta}}{\sqrt{2k}}, \quad T'_{R,L} = -ik\,T_{R,L}. \tag{3.2}$$

The same initial conditions are used for $\psi_{R,L}$. To discard the contributions from quantum vacuum fluctuations of $T_{R,L}$ in the calculation of the integrals in (2.35) and (2.36), we use the criterion that for wave numbers where $|T_{R,L}|^2 < 1/2k$, the value of $|T_{R,L}|^2$ is replaced by zero.

3.2 New late-time attractor solution

We have performed a range of simulations with different values of μ, g, and λ; see Appendix A for a summary. When μ and therefore also m_Q are large enough, the system undergoes a transition to a new late-time attractor with negative values of Q after about $N = 2$–10 e-folds; see figure 2. [**OI**: mention χ evolution]

For the test of our numerical implementation, we choose the initial value of μ and g for one of the runs such that the backreaction of the perturbations on the background evolution is negligible. Run $\mu1$ is an example of such a case. It is evident from figure 2 that Q remains constant in time for run $\mu1$, as expected from the analytical results. Furthermore, we have compared our numerical results for the $\sqrt{2k}\langle x|T_{R,L}|\rangle$ and $\sqrt{2k}\langle x|\psi_{R,L}|\rangle$ with the analytically expected results and show the comparison in the upper panel of figure 3 for $k = 10^{-4}$. In this figure, the red and blue curves show the numerical result for the right and left-handed

polarization respectively and the green curve shows the analytic solution obtained using the homogeneous solution of the T_R Equation (2.25). This solution is given by [14],

$$T_R = \frac{1}{\sqrt{2k}} i^{\beta} W_{\beta,\alpha}(2ik\eta). \tag{3.3}$$

Here, $W_{\beta,\alpha}(2ik\eta)$ is the Whittaker function with $\beta = -i(m_Q + \xi)$, and $\alpha = -i\sqrt{2m_Q\xi - 1/4}$. The Whittaker solution provides a good analytical solution for T_R for a particular wave number approximately until the Hubble horizon crossing. However, the solution starts to differ in the deep super Hubble horizon regime due to the contribution from the metric tensor perturbations. It is evident from the upper panel of figure 3 that our numerical solution matches well with the analytically expected one in the regime where the analytical solution is valid.

In figure 2, we show the time evolution of Q and χ for simulations $\mu 1$, $\mu 4$, and $\mu 5$ having different values of μ that corresponds to $m_{Q_0} = 2.44, 3.0$, and 3.58. For the run where $m_{Q_0} = 3.58$, the backreaction of the perturbations becomes important, and because of this, Q starts to change with time. However, it stabilizes to another constant value at a later time. We show the evolution of the $\sqrt{2k}(x|T_{R,L}|)$ and $\sqrt{2k}(x|\psi_{R,L}|)$ for this run in the middle panel of figure 3 and the evolution of the integrand of the backreaction integrals $\mathcal{T}^{Q}_{\rm BR}$ and $\mathcal{T}^{\chi}_{\rm BR}$ in figure 4. Here $x = -k\eta$ is the dimensionless time variable.

From figure 4, we conclude that most of the contribution to the backreaction comes from a fixed narrow range of wave numbers. This range is different for different values of m_Q. For the run $\mu 3$, the range is around $\ln k/(a_0 H) \approx 10$ and for the run $\mu 5$, it is $\ln k/(a_0 H) \approx 3$. We also consider variable k range for these runs. However, these runs lead to some unphysical oscillatory features in the background evolution as shown in Appendix B. [**OI**: Comment on superhozion mode]

3.3 Semi-analytical modelling

In this section, we provide a semi-analytical analysis to approach the new attractor solution at late times. In order to provide some intuition on dynamics in the backreaction regime, it is instructive to investigate the evolution of each contribution to equations of motion (2.33)–(2.34). The time dependence of contributions is shown in figure 5. Following the evolution of the backreaction terms $\mathcal{T}^{Q}_{\rm BR}$, $\mathcal{T}^{\chi}_{\rm BR}$, three distinct phases of dynamics can be distinguished. From the top left and bottom left panels of figure 5 one can see that the backreaction contributions (solid black curves) grow exponentially in absolute value up to around 8 e-folds. We will refer to the stage of exponential growth of backreaction as Stage I. When the backreaction contributions become comparable to one of the terms in the equations of motion, Stage II begins. At this stage, the backreaction terms change their behavior, start to decrease, and eventually cross zero. Following this stage, the system converges to the final solution (the top right and bottom right panels of figure 5) which we refer to as Stage III. The dynamics during different stages is described in more detail in Appendix C.

Let us turn right away to the discussion of the new late-time dynamical attractor. At Stage III, all the contributions to equations of motion become nearly constant. In addition, the term $-(g\lambda/f)\, a\chi' Q^2$ becomes nearly equal to the contribution $2\mathcal{H}^2 Q$ in the equation of motion (2.33)[1], that leads to

$$\frac{\lambda}{af}\chi' \simeq -\frac{2H^2}{gQ}, \qquad Q \simeq \text{const.} \tag{3.4}$$

[1]We used $\mathcal{H}' = a^2\dot{H} + \mathcal{H}^2$ and $\dot{H} = 0$ in numerical simulations.

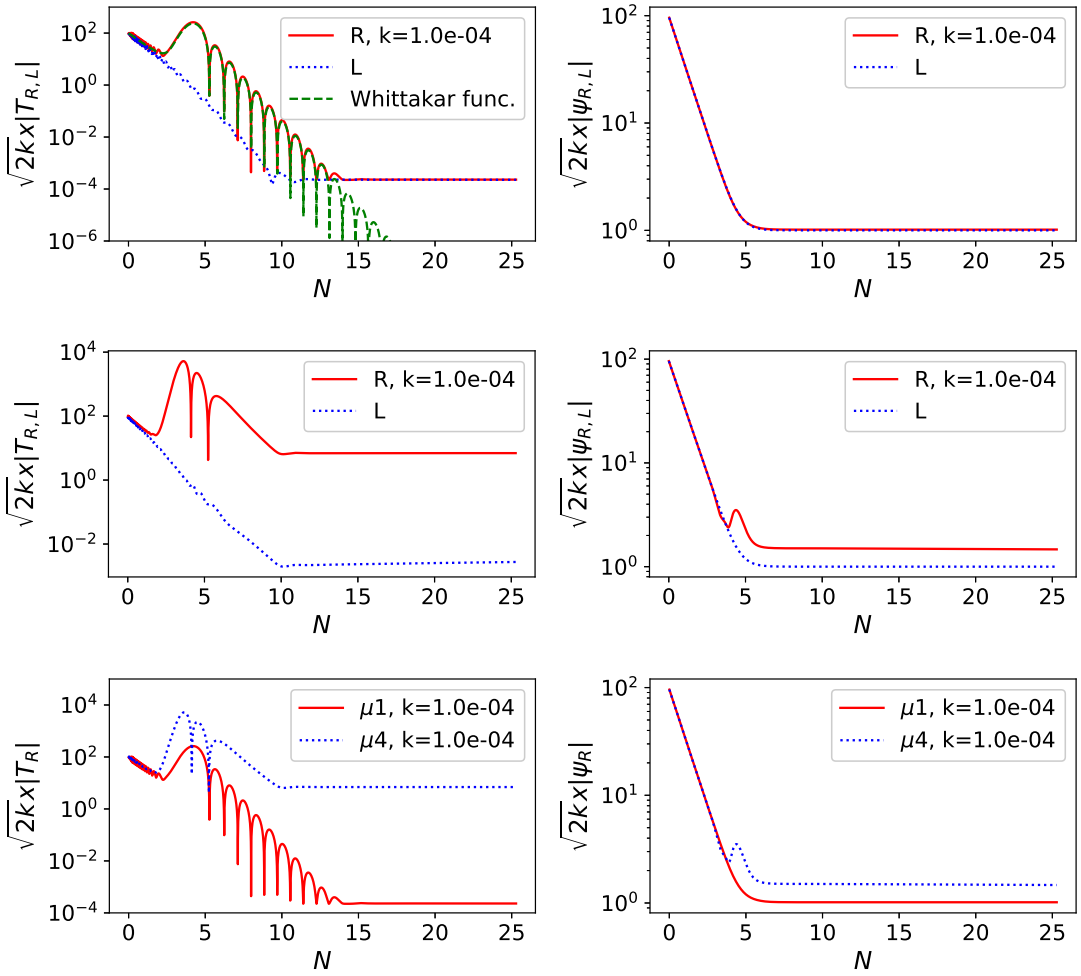

Figure 3. $\sqrt{2k}x|T_{R,L}|$ and $\sqrt{2k}x|\psi_{R,L}|$ vs N for $k = 10^{-4}$ for Runs $\mu 1$ (top panel), μ (middle panel). In the top and middle panels, the red and blue curves represent the numerical results for the right and left-handed polarization respectively. In bottom panel we show a comparison between of $\sqrt{2k}x|T_R|$ and $\sqrt{2k}x|\psi_R|$ for the runs $\mu 1$ and $\mu 4$. [**OI**: "Whittaker", not "WhittakAr" in the legend. I think we can remove a lower panel and also $k = 1.0e-04$ from legends since it is the same for all plots.]

This solution resembles the original chromo-natural attractor solution given in Eq. (2.15) with $Q = \text{const}$ and just with the second term present that has an opposite sign. It follows on the late-time attractor $\xi \simeq -1/m_Q$. In figure 6, we show that Equation (3.4) does indeed hold. With (3.4), the equations of motion on Stage III become

$$4H^2Q + 2g^2Q^3 + \mathcal{T}^Q_{\rm BR} \simeq 0, \tag{3.5}$$

$$U_\chi + \frac{3g\lambda}{f}HQ^3 + \mathcal{T}^\chi_{\rm BR} \simeq 0, \tag{3.6}$$

where we have taken into account that terms with derivatives at the last stage are negligible.

Let us now take a closer look into the time dependence of each component of the backreaction integrals (2.35) and (2.36). Backreaction terms may be written in conformal

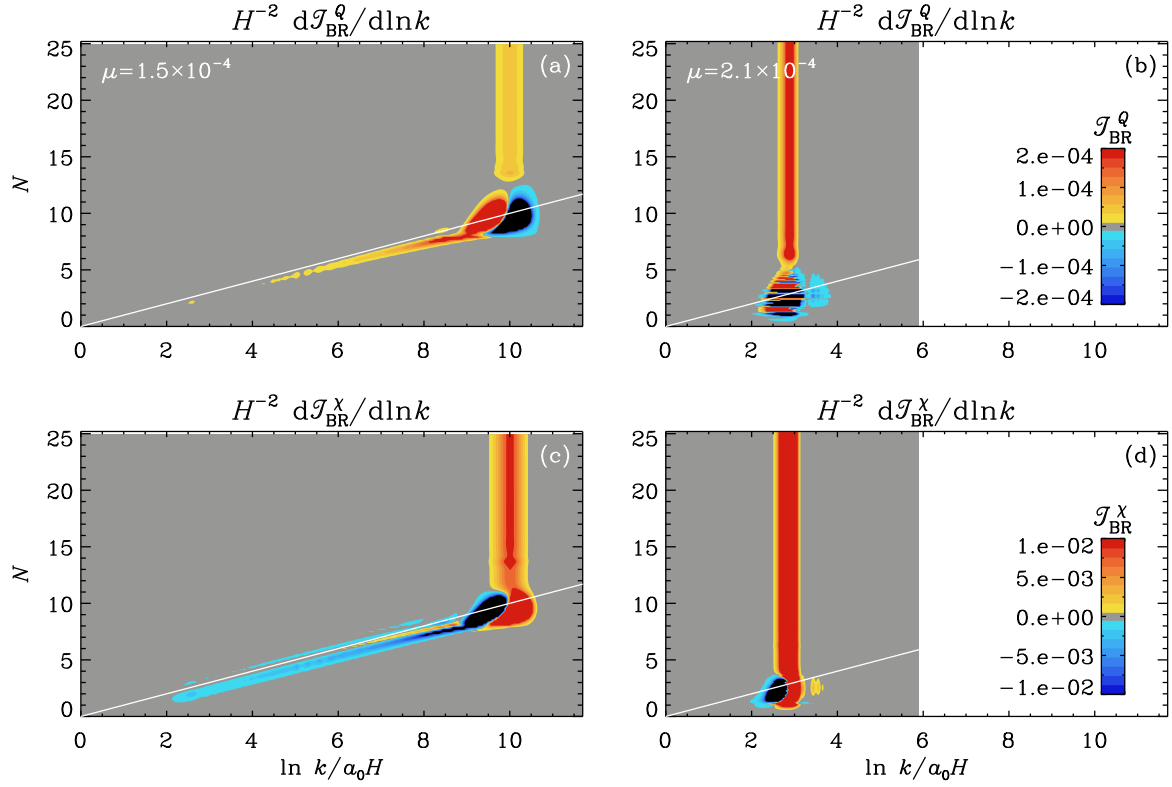

Figure 4. The integrands of $\mathcal{T}^{Q}_{\rm BR}$ and $\mathcal{T}^{\chi}_{\rm BR}$, denoted here by $d\mathcal{T}^{Q}_{\rm BR}/d\ln k$ and $d\mathcal{T}^{\chi}_{\rm BR}/d\ln k$, respectively, for $\mu = 1.5\times10^{-4}$ (Run $\mu3$) and $\mu = 2.1\times10^{-4}$ (Run $\mu5$). The white line indicates the position of the comoving horizon.

time as

$$\mathcal{T}^{Q}_{\rm BR} = \frac{g}{3a^2}\left(\xi H\langle|T|^2\rangle - \frac{1}{a}\langle k|T|^2\rangle\right) \equiv \mathcal{T}^{Q}_{1} + \mathcal{T}^{Q}_{2}, \tag{3.7}$$

$$\mathcal{T}^{\chi}_{\rm BR} = -\frac{\lambda}{2a^3 f}\left[m_Q H\langle|T|^2\rangle' - \frac{1}{a}\langle k|T|^2\rangle' + \left(am_Q H^2 + gQ'\right)\langle|T|^2\rangle\right] = \tag{3.8}$$

$$\equiv \mathcal{T}^{\chi}_{1} + \mathcal{T}^{\chi}_{2} + \mathcal{T}^{\chi}_{3} + \mathcal{T}^{\chi}_{4}, \tag{3.9}$$

where we have denoted the integrals over wave numbers by

$$\langle|T|^2\rangle = \int \frac{d^3k}{(2\pi)^3}\left(|T_R|^2 + |T_L|^2\right), \quad \langle k|T|^2\rangle = \int \frac{d^3k}{(2\pi)^3}\, k\left(|T_R|^2 - |T_L|^2\right). \tag{3.10}$$

It is worth noting that in all our cases, the contributions from $|T_L|$ are negligible. In figure 7, we show the time evolution of the different contributions to the $\mathcal{T}^{Q}_{\rm BR}$ and $\mathcal{T}^{\chi}_{\rm BR}$ integrals. There is a clear correspondence between the background dynamics and backreaction integrals, and vice versa. We refer the interested reader to the detailed discussion in Appendix C.

The backreaction integrals include crucial information that governs the evolution of the whole system. It is therefore convenient to introduce a new parameter that quantifies the ratio of two backreaction integrals

$$\frac{\mathcal{T}^{Q}_{\rm BR}}{\mathcal{T}^{\chi}_{\rm BR}} \equiv \alpha. \tag{3.11}$$

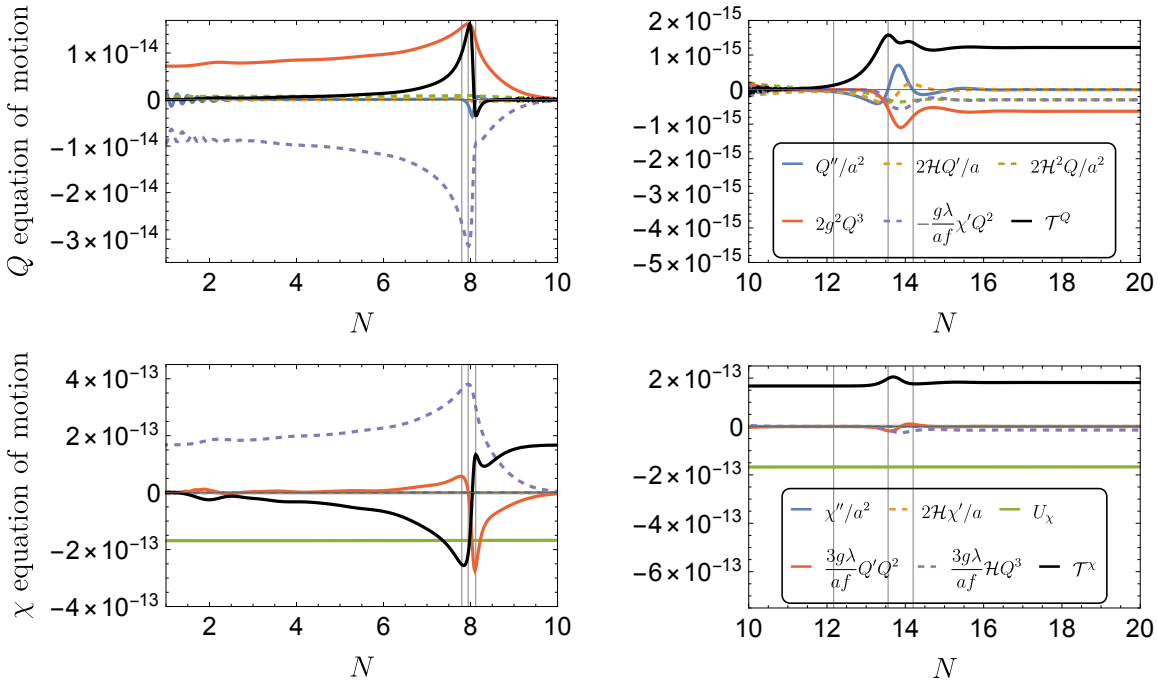

Figure 5. *Top left*: Contributions to the equation of motion for the VEV of the gauge field, Q, with respect to the number of e-folds at the initial stage and when backreaction is turned on. The three vertical gray grid lines correspond to the moments when $Q'' = 0$, $Q' = 0$, and then again $Q'' = 0$ (from left to right) respectively. *Top right*: Contributions to the equation of motion for Q during the transition to the final attractor solution. Vertical gray grid lines correspond to the moments when $Q = 0$, $Q'' = 0$, $Q'' = 0$ (from left to right) respectively. *Bottom left*: Contributions to the equation of motion for the axion field, χ, with respect to the number of e-folds at the initial stage and when backreaction is turned on. Grid lines are the same as in the top left panel. *Bottom right*: Contributions to the equation of motion for χ during the transition to the final attractor solution. Grid lines are the same as in the top right panel.

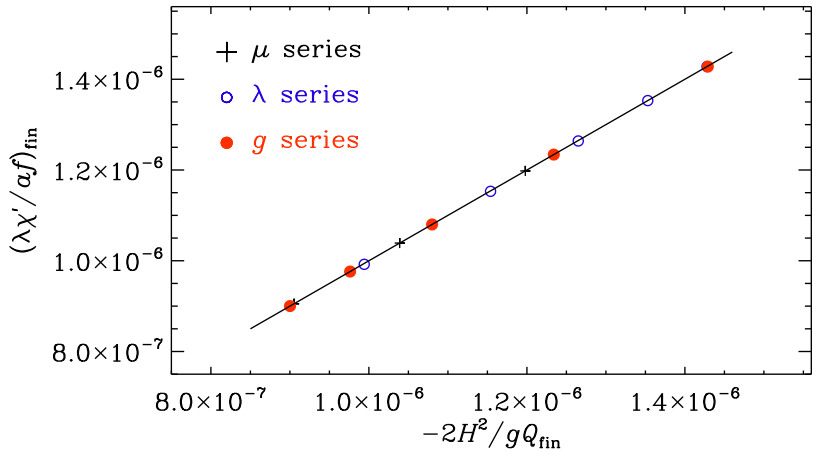

Figure 6. Verification of equation (3.4), showing $(\lambda\chi'/af)_{\rm fin}$ versus $-2H^2/gQ_{\rm fin}$, where $Q_{\rm fin}$ denotes the value of Q at the final attractor for multiple series of runs from table 1.

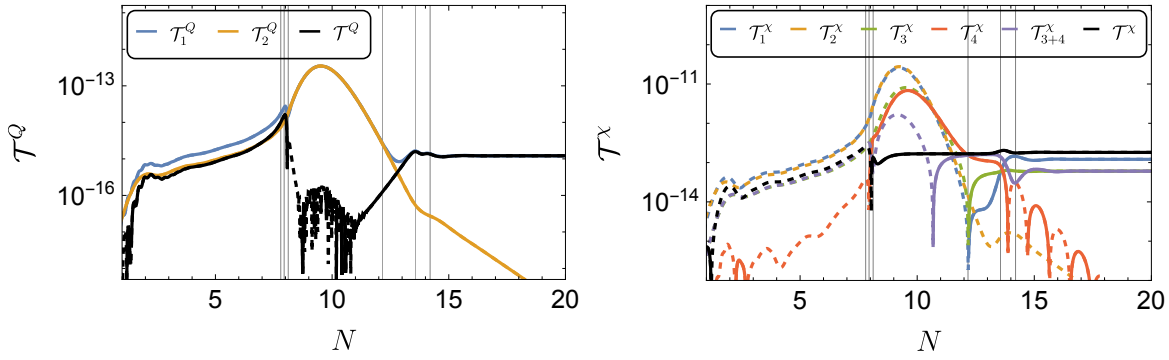

Figure 7. *Left*: Backreaction terms $\mathcal{T}^Q_{\rm BR}$ and their contributions with respect to the number of e-folds. *Right*: Backreaction terms $\mathcal{T}^\chi_{\rm BR}$ with contributions with respect to the number of e-folds. Grid lines are the same as in figure 5.

From equations (3.5)–(3.6), one can find the relation between χ and Q on the final attractor

$$U_\chi = -\frac{3g\lambda}{f} H Q^3 + \frac{1}{\alpha}\left(4H^2 Q + 2g^2 Q^3\right). \tag{3.12}$$

At the final stage it holds $\mathcal{T}^Q_{\rm BR} \simeq \mathcal{T}^Q_1$ and $\mathcal{T}^\chi_{\rm BR} \simeq \mathcal{T}^\chi_1 + \mathcal{T}^\chi_3$, therefore, the parameter α can be expressed as

$$\alpha = \frac{2}{9}\frac{Hf}{\lambda g\, Q^2_{\rm fin}}, \tag{3.13}$$

where we used $\langle |T|^2\rangle' \simeq 2aH\langle |T|^2\rangle$ and $Q_{\rm fin}$ denotes the value of Q at the final attractor. The dependence of α on the parameters λ, g, and μ is confirmed in figure 8 for runs of the three families. To sum up, the late-time dynamical attractor is given by equations (3.4), (3.12) and (3.13).

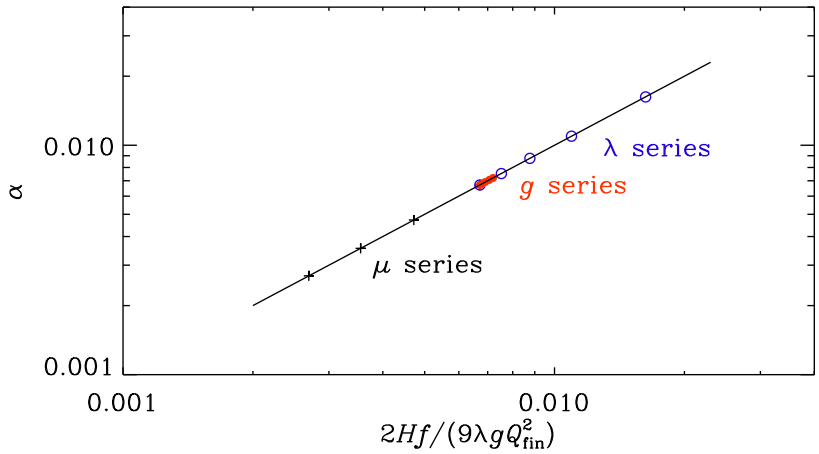

Figure 8. Dependence of the parameter α versus $Q_{\rm fin}$ for three series of runs.

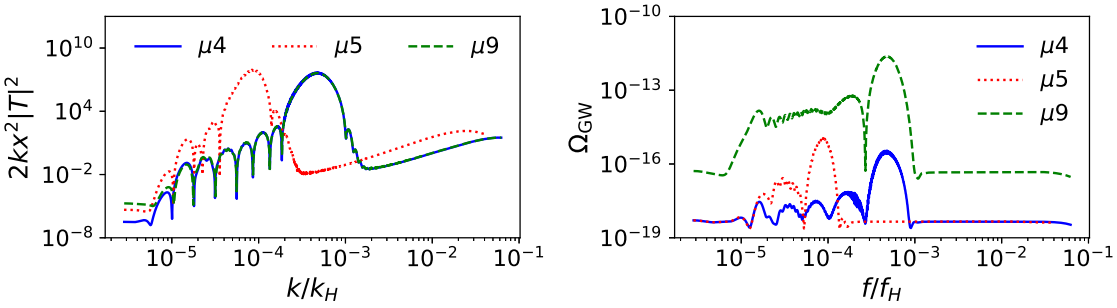

Figure 9. $2kx^2|T|^2$ vs k/k_H and $\Omega_{\rm GW}$ vs f/f_H is shown for the runs $\mu4$, $\mu5$ and $\mu9$.

3.4 Observational signatures

The GW energy density power spectrum can be approximated as [21]

$$\Omega_{\rm GW}(k) = \frac{3}{128}\Omega_{\rm rad}\mathcal{P}_h^{\rm tot}(k)\left[\frac{1}{2}\left(\frac{k_{\rm eq}}{k}\right)^2 + \frac{16}{9}\right], \tag{3.14}$$

where $\Omega_{\rm rad} \simeq 2.47 \times 10^{-5}$ is the present radiation density parameter and $k_{\rm eq} \simeq 1.3 \times 10^{-2}\,{\rm Mpc}^{-1}$ is the wave number entering the horizon at matter-radiation equality. To express $\Omega_{\rm GW}$ as a function of frequency, we use $f \simeq 1.5 \times 10^{-15}\,(k/{\rm Mpc}^{-1})\,{\rm Hz}$.

In figure 9, we show $2kx^2|T|^2$ vs k/k_H, and $\Omega_{\rm GW}$ vs f/f_H for the runs $\mu1$ and $\mu5$, respectively. The upper and lower panels correspond to the run $\mu1$ and $\mu5$, respectively. In this figure, we have normalized the wave number and GW frequency using the values corresponding to the Hubble horizon size (k_H) at the end of inflation and the corresponding frequency (f_H). These quantities are given by

$$k_H = \frac{a_e}{a_0}H = 2.3 \times 10^{22}{\rm Mpc}^{-1}, \quad f_H = \frac{k_H}{2\pi} = 3.5 \times 10^{7}{\rm Hz}. \tag{3.15}$$

Here, $H = 1.04 \times 10^{-6} M_{\rm Pl}$ and we assume the adiabatic evolution of the Universe to calculate a_e/a_0, given by

$$\frac{a_e}{a_0} = \left(\frac{g_{0s}}{g_{rs}}\right)^{1/3}\frac{T_0}{T_r} = 5.8 \times 10^{-29}\frac{g_{0s}}{3.94}\frac{106.75}{g_{rs}}\frac{T_0}{2.73{\rm K}}\frac{1.3 \times 10^{15}}{T_r}. \tag{3.16}$$

In the above expression, g_{*s} and g_{0s} denote the effective degrees of freedom in the entropy at the end of inflation and the present epoch, respectively, and T_r denotes the reheating temperature assuming instantaneous reheating. We estimate T_r by using the relation $3H^2M_{\rm Pl}^2 = (\pi^2/30)g_r T_r^4$.

As is evident from figure 9, the modes that are amplified around horizon crossing give the largest values of $\Omega_{\rm GW}$.

4 Summary and discussion

In this work, we simulated an axion-SU(2) sector, which is a spectator during inflation, meaning that its energy density is subdominant to the inflaton and that both the Hubble rate

and the density perturbations are unaffected by its presence. The simulations are performed in what can be called the mild backreaction regime. This is because the fluctuations are computed using the linearized equations of motion, even though their effect on the axion and gauge field VEV is computed self-consistently, but averaged over the simulation domain. This method is similar in spirit to the one followed in ref. [3] in the case of axion-$U(1)$ inflation, where the gauge fields are computed using linear equations of motion and their collective effect is considered a background quantity and added to the corresponding background equations. In the case of the Abelian model, an oscillatory result was found that can be understood in the following way: an increase in axion velocity leads to an increase in the gauge field amplification. This results in an increased backreaction on the rolling axion through the $\langle \mathbf{E} \cdot \mathbf{B} \rangle$ term. This backreaction leads to a slow-down of the axion, which, in turn, reduces the subsequent amplification of gauge fields. Since the gauge fields are already produced red-shifted, their backreaction will also reduce, leading to a speed-up of the axion and the whole process will start anew, thus leading to periodic bursts of gauge field production.

In the non-Abelian case, the initial stage is similar to the Abelian case: as the axion picks up speed, the gauge fields (a tensor mode in this case) are exponentially amplified. This leads to a backreaction on the equations of motion that define the VEV of both the axion field as well as the SU(2) sector. This leads to both a slow-down of the axion, as well as a completely new sign-flipped value for the gauge field VEV. Furthermore, in this new regime, the super-horizon tensor modes of the gauge field do not redshift, as expected, but are instead constant [ES:right?]. This leads to the absence of the periodic behavior found in the Abelian case, because the backreaction of the gauge field fluctuations onto the background quantities does not diminish with time (to the lowest order in slow-roll).

Having revealed this new regime, several questions remain to be answered. An intriguing relation was found between the backreaction terms in the axion and gauge VEVs, leading to a universal relation between the parameters of the potential and the late-time value of the gauge VEV. However, we are not able to predict the gauge VEV itself in this new attractor. We believe that the initial value of the gauge VEV (in the original chromo-natural attractor) plays a role in determining its late-time value.

Furthermore, our analysis neglects spatially dependent backreaction effects that can lead to mode-mode coupling of the gauge field, as well as the excitation of scalar fluctuations in the axion sector. It has been shown in ref. [7] that space-dependent backreaction effects can be very important in the Abelian case. It is thus important to revisit our calculation, solving the full system on a lattice, without making any linear or Hartree-type approximations.

Furthermore, our calculation was performed with a constant Hubble scale, in an exact de-Sitter background. While this can be an excellent approximation for several inflationary models, it does not allow us to probe the evolution of this new attractor close to the end of inflation, where $|\dot{H}/H^2| \sim 1$.

Finally, the flipped sign of the gauge field VEV provides the possibility of amplifying the subdominant helicity of gauge tensor modes. Further analysis of this is left for future work, as it can provide interesting scale-dependent observables.

... these retardation effects are not present. When the [ES: which are the dominant terms in the gauge field eoms?] [**OI**: See Fig. 5]

Acknowledgments

The work of O.I. was supported by the European Union's Horizon 2020 research and innovation program under the Marie Skodowska-Curie grant agreement No. 101106874. R.S. was supported through grant No. ERC HERO-810451 from the European Research Council. A.B. acknowledges the grants No. 2019-04234 from the Swedish Research Council (Vetenskapsrådet) and the ASA ATP grant No. 80NSSC22K0825. O.I. is grateful to the University of Leiden for hospitality where parts of this work have been completed. We thank the Swedish National Allocations Committee for providing computing resources at the Center for Parallel Computers at the Royal Institute of Technology in Stockholm and the National Supercomputer Centre (NSC) at Linköping. Nordita was sponsored by Nordforsk.

Run	μ	g	λ	m_{Q_0}	Q_0	$Q_{\rm fin}$	α
$\mu1$	1.20×10^{-4}	1.11×10^{-2}	500	2.44	2.29×10^{-4}	2.26×10^{-4}	-1.67×10^{-2}
$\mu2$	1.40×10^{-4}	1.11×10^{-2}	500	3.00	2.81×10^{-4}	2.77×10^{-4}	-1.59×10^{-2}
$\mu3$	1.50×10^{-4}	1.11×10^{-2}	500	3.29	3.08×10^{-4}	-1.36×10^{-4}	6.71×10^{-3}
$\mu4$	1.60×10^{-4}	1.11×10^{-2}	500	3.58	3.36×10^{-4}	-1.45×10^{-4}	5.91×10^{-3}
$\mu4$'	1.60×10^{-3}	1.11×10^{-2}	500	77.2	7.23×10^{-3}	-1.46×10^{-3}	5.90×10^{-4}
$\mu5$	1.80×10^{-4}	1.11×10^{-2}	500	4.19	3.93×10^{-4}	-1.63×10^{-4}	4.72×10^{-3}
$\mu6$	1.90×10^{-4}	1.11×10^{-2}	500	4.51	4.22×10^{-4}	-1.71×10^{-4}	4.27×10^{-3}
$\mu7$	2.10×10^{-4}	1.11×10^{-2}	500	5.15	4.82×10^{-4}	-1.88×10^{-4}	3.55×10^{-3}
$\mu8$	2.45×10^{-4}	1.11×10^{-2}	500	6.32	5.92×10^{-4}	-2.15×10^{-4}	2.70×10^{-3}
$g1$	1.50×10^{-4}	1.11×10^{-2}	500	3.29	3.08×10^{-4}	-1.36×10^{-4}	6.71×10^{-3}
$g2$	1.50×10^{-4}	1.50×10^{-2}	500	4.02	2.79×10^{-4}	-1.17×10^{-4}	6.77×10^{-3}
$g3$	1.50×10^{-4}	2.00×10^{-2}	500	4.87	2.53×10^{-4}	-1.00×10^{-4}	6.91×10^{-3}
$g4$	1.50×10^{-4}	2.50×10^{-2}	500	5.65	2.35×10^{-4}	-8.86×10^{-5}	7.06×10^{-3}
$g5$	1.50×10^{-4}	3.00×10^{-2}	500	6.38	2.21×10^{-4}	-8.01×10^{-5}	7.20×10^{-3}
$\lambda1$	1.50×10^{-4}	1.11×10^{-2}	600	3.09	2.90×10^{-4}	2.87×10^{-4}	-1.31×10^{-2}
$\lambda2$	1.50×10^{-4}	1.11×10^{-2}	500	3.29	3.08×10^{-4}	-1.36×10^{-4}	6.71×10^{-3}
$\lambda3$	1.50×10^{-4}	1.11×10^{-2}	400	3.54	3.32×10^{-4}	-1.44×10^{-4}	7.53×10^{-3}
$\lambda4$	1.50×10^{-4}	1.11×10^{-2}	300	3.90	3.65×10^{-4}	-1.54×10^{-4}	8.77×10^{-3}
$\lambda5$	1.50×10^{-4}	1.11×10^{-2}	200	4.46	4.18×10^{-4}	-1.69×10^{-4}	1.10×10^{-2}
$\lambda6$	1.50×10^{-4}	1.11×10^{-2}	100	5.62	5.27×10^{-4}	-1.96×10^{-4}	1.62×10^{-2}

Table 1. Summary of runs for the g, λ, and μ series. For each series, the first line refers to the fiducial run with $\mu=1.5\times10^{-4}$, $g=1.11\times10^{-2}$, and $\lambda=500$. Run $\mu4$' is the same as Run $\mu4$, except that here $H=1.04\times10^{-5}$ is 10 times larger than usual.

A Full set of parameters

The full set of parameters used in the simulations is shown in Table 1. The fiducial parameters are $\mu=1.5\times10^{-4}$, $g=1.11\times10^{-2}$, and $\lambda=500$. The runs are grouped separately for runs $\mu1$–$\mu8$ with $1.2\leq\mu/10^{-4}\leq2.45$, runs $g1$–$g5$ with $1.11\leq g/10^{-2}\leq3$, and runs $\lambda1$–$\lambda6$ with $100\leq\lambda\leq600$. Only the runs with negative values of $Q_{\rm fin}$ have undergone backreaction.

B Artifacts from not resolving the superhorizon modes

One might have expected that it is important to resolve the modes around the comoving horizon. Looking at figure 4, this is not obvious, however. Once backreaction becomes important, most of the contributions to the backreaction come from a fixed band of wave numbers. It is instructive to examine the results where we allow for the possibility to move the range of integration to a comoving strip with

$$n_{\rm min}\leq\ln[k/a(\eta)H]\leq n_{\rm max}. \tag{B.1}$$

The result of numerical simulation using a comoving strip of wave numbers is shown in figure 10.

As we see from the insets of figure 10, the corresponding evolution of Q is different in cases where the modes in the proximity of the comoving horizon are resolved at the expense of

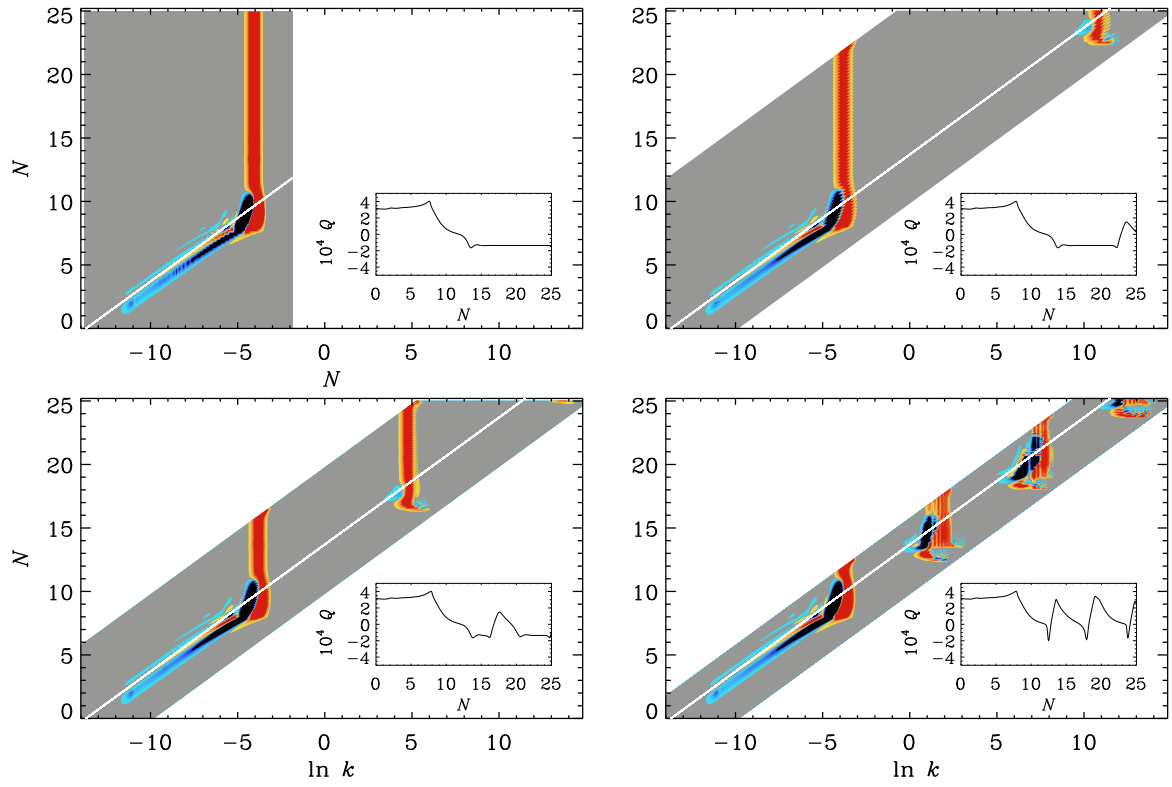

Figure 10. $\mathcal{T}^Q_{\rm BR}$ for $(Q_0, \mu)/10^{-4} = (3.2,\, 1.5)$ without shift for $0 \leq \ln k \leq 12$ (first panel), and with shift for $-12 \leq \ln k/aH \leq 4$, $-12 \leq \ln k/aH \leq 4$, $-6 \leq \ln k/aH \leq 4$, and $-2 \leq \ln k/aH \leq 4$ (the other 3 panels). The insets show the corresponding evolution of Q.

not capturing any more the strongly super-horizon modes. We can conclude that this causes numerical artifacts that look like periodic bursts of gauge field production during inflation.

C Detailed description of backreaction stages

At the initial stage, referred to here as Stage I, the solution follows the chromo-natural attractor solution (2.15), where the three terms $-(g\lambda/af)\chi' Q^2$, $2g^2Q^3$, and $2\mathcal{H}^2Q/a^2$ balance each other in (2.33). Note that, in the present case of $H = \text{const}$, we have $\mathcal{H}' + \mathcal{H}^2 = 2\mathcal{H}^2$. When the backreaction $\mathcal{T}^Q_{\rm BR}$ becomes important, the contribution $-(g\lambda/af)\,\chi' Q^2$ becomes more dominant compared to the rest of the terms (see purple dashed curve in the top left and bottom left of figure 5). To compensate for the increase of the sum $\mathcal{T}^Q_{\rm BR}$ and $-(g\lambda/af)\,\chi' Q^2$ terms, the Q'' contribution becomes negative. It causes the change in the sign of Q'. This changes the behavior and turns on the Q' term, $\mathcal{T}^\chi_4$, in the integral $\mathcal{T}^\chi_{\rm BR}$ of Equation (3.9), which produces a bump in ξ; see figure 11. This happens around $N = 8$ e-folds. The change in ξ makes the two terms $\mathcal{T}^Q_1$ and $\mathcal{T}^Q_2$ in (3.7) almost cancel each other, see figure 7. As a result, the $\mathcal{T}^Q_{\rm BR}$ term becomes first negative and is then close to zero. This causes a decrease of Q. The steps at Stage I can be described by the following chain sequence:

$$\mathcal{T}^Q_{\rm BR} \to Q'' \to Q' \to \mathcal{T}^\chi_{\rm BR} \to \xi(\chi') \to \mathcal{T}^Q_{\rm BR} \to Q.$$

Stage I	Stage II	Stage III
$\mathcal{T}^Q_{\rm BR} \propto \exp(\mathcal{O}(1)N)$ $\lvert\mathcal{T}^\chi_{\rm BR}\rvert \propto \exp(\mathcal{O}(1)N)$	$\mathcal{T}^Q_{\rm BR} \approx 0$ $U_\chi + (3g\lambda/f)HQ^3 + \mathcal{T}^\chi_{\rm BR} \simeq 0$	$4H^2Q + 2g^2Q^3 + \mathcal{T}^Q_{\rm BR} \simeq 0$ $U_\chi + (3g\lambda/f)HQ^3 + \mathcal{T}^\chi_{\rm BR} \simeq 0$

Table 2. The three stages of dynamics in axion-SU(2) inflation with backreaction.

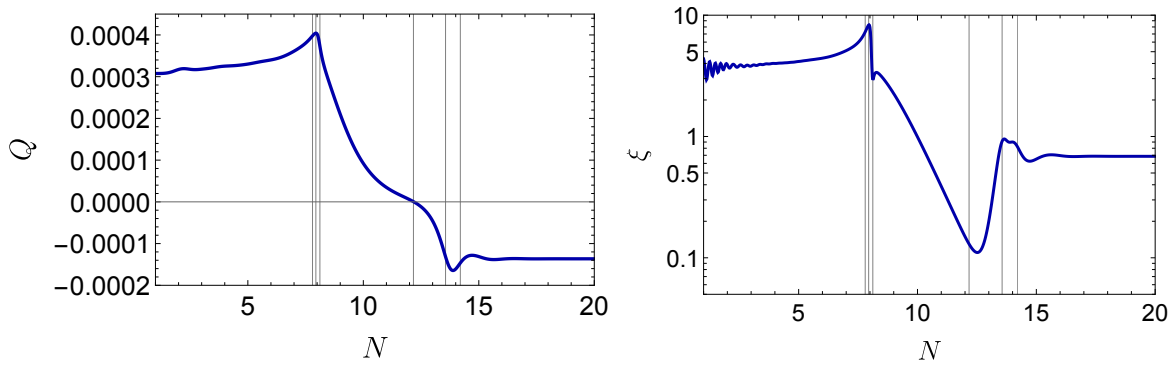

Figure 11. *Left*: The VEV of the gauge field Q versus the number of e-folds. Grid lines are the same as in figure 5. *Right*: The evolution of ξ parameter defined in equation (2.17) with respect to the number of e-folds.

The next stage, Stage II, is characterized by a continuous decrease of Q. The backreaction $\mathcal{T}^Q_{\rm BR} \approx 0$ remains small, and $\mathcal{T}^\chi_{\rm BR} \approx$ const.

The last stage, Stage III, begins when the gauge field VEV reaches zero, i.e., $Q = 0$. This changes the sign of terms with m_Q, i.e., $\mathcal{T}^\chi_1$ and $\mathcal{T}^\chi_3$ from (3.9). This governs the change in ξ and causes the inflection of the $\mathcal{T}^Q_1$ contribution. As a result, the solution arrives at the final attractor (3.4) with $\mathcal{T}^\chi = \mathcal{T}^\chi_1 + \mathcal{T}^\chi_3 \approx$ const and $\mathcal{T}^Q = \mathcal{T}^Q_1 \approx$ const. At Stage III, we observe the following chain sequence:

$$Q \to m_Q \to \mathcal{T}^\chi_{\rm BR} \to \xi(\chi') \to \mathcal{T}^Q_{\rm BR} \to Q.$$

The three stages of evolution are summarized in Table 2.

D Example plots (only for the draft)

References

[1] K. Freese, J.A. Frieman and A.V. Olinto, *Natural inflation with pseudo - Nambu-Goldstone bosons*, *Phys. Rev. Lett.* **65** (1990) 3233.

[2] F.C. Adams, J.R. Bond, K. Freese, J.A. Frieman and A.V. Olinto, *Natural inflation: Particle physics models, power law spectra for large scale structure, and constraints from COBE*, *Phys. Rev. D* **47** (1993) 426 [hep-ph/9207245].

[3] J. Garcia-Bellido, A. Papageorgiou, M. Peloso and L. Sorbo, *A flashing beacon in axion inflation: recurring bursts of gravitational waves in the strong backreaction regime*, 2303.13425.

[4] R. von Eckardstein, M. Peloso, K. Schmitz, O. Sobol and L. Sorbo, *Axion inflation in the strong-backreaction regime: decay of the Anber-Sorbo solution*, 2309.04254.

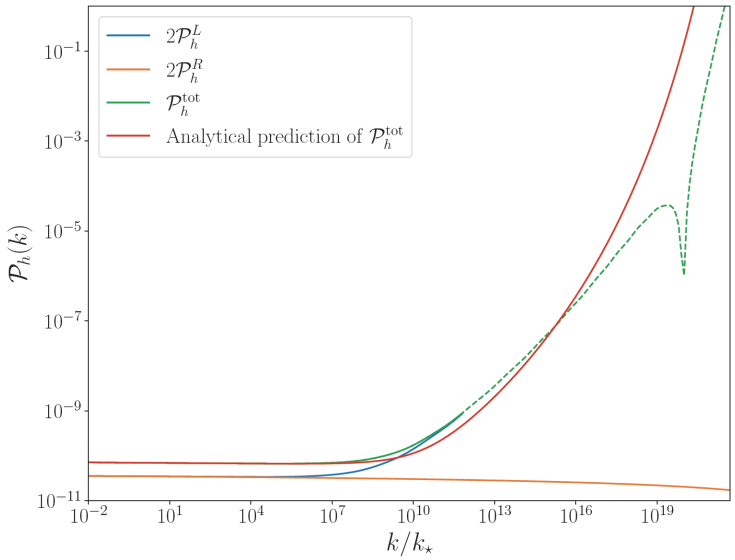

Figure 12. Example plot of tensor power spectrum.

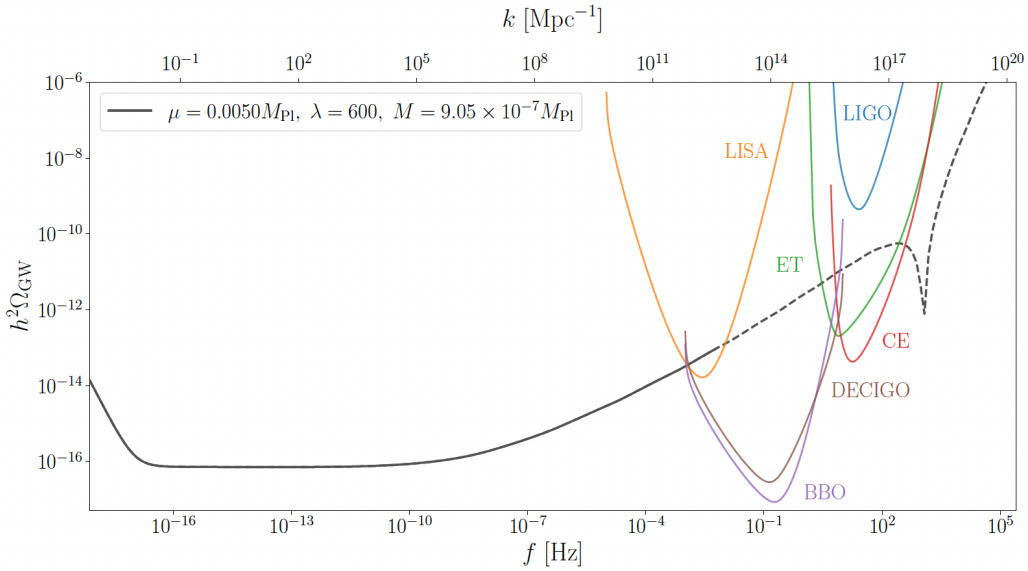

Figure 13. Example plot of $\Omega_{\rm GW}$.

[5] M. Peloso and L. Sorbo, *Instability in axion inflation with strong backreaction from gauge modes*, *JCAP* **01** (2023) 038 [2209.08131].

[6] A. Caravano, E. Komatsu, K.D. Lozanov and J. Weller, *Lattice simulations of axion-U(1) inflation*, *Phys. Rev. D* **108** (2023) 043504 [2204.12874].

[7] D.G. Figueroa, J. Lizarraga, A. Urio and J. Urrestilla, *The strong backreaction regime in axion inflation*, 2303.17436.

[8] T. Fujita, K. Mukaida, K. Murai and H. Nakatsuka, *SU(N) natural inflation*, *Phys. Rev. D* **105** (2022) 103519 [2110.03228].

[9] P. Adshead, E. Martinec and M. Wyman, *Perturbations in Chromo-Natural Inflation*, *JHEP* **09** (2013) 087 [1305.2930].

[10] P. Adshead, E. Martinec and M. Wyman, *Gauge fields and inflation: Chiral gravitational waves, fluctuations, and the Lyth bound*, *Phys. Rev. D* **88** (2013) 021302 [1301.2598].

[11] P. Adshead and M. Wyman, *Chromo-Natural Inflation: Natural inflation on a steep potential with classical non-Abelian gauge fields*, *Phys. Rev. Lett.* **108** (2012) 261302 [1202.2366].

[12] A. Maleknejad, *Axion Inflation with an SU(2) Gauge Field: Detectable Chiral Gravity Waves*, *JHEP* **07** (2016) 104 [1604.03327].

[13] P. Adshead, E. Martinec, E.I. Sfakianakis and M. Wyman, *Higgsed Chromo-Natural Inflation*, *JHEP* **12** (2016) 137 [1609.04025].

[14] E. Dimastrogiovanni, M. Fasiello and T. Fujita, *Primordial Gravitational Waves from Axion-Gauge Fields Dynamics*, *JCAP* **01** (2017) 019 [1608.04216].

[15] T. Fujita, E.I. Sfakianakis and M. Shiraishi, *Tensor Spectra Templates for Axion-Gauge Fields Dynamics during Inflation*, *JCAP* **05** (2019) 057 [1812.03667].

[16] A. Maleknejad and E. Erfani, *Chromo-Natural Model in Anisotropic Background*, *JCAP* **03** (2014) 016 [1311.3361].

[17] E. Dimastrogiovanni and M. Peloso, *Stability analysis of chromo-natural inflation and possible evasion of Lyth's bound*, *Phys. Rev. D* **87** (2013) 103501 [1212.5184].

[18] A. Papageorgiou, M. Peloso and C. Unal, *Nonlinear perturbations from axion-gauge fields dynamics during inflation*, *JCAP* **07** (2019) 004 [1904.01488].

[19] T. Fujita, R. Namba and Y. Tada, *Does the detection of primordial gravitational waves exclude low energy inflation?*, *Phys. Lett. B* **778** (2018) 17 [1705.01533].

[20] Pencil Code Collaboration, A. Brandenburg, A. Johansen, P. Bourdin, W. Dobler, W. Lyra et al., *The Pencil Code, a modular MPI code for partial differential equations and particles: multipurpose and multiuser-maintained*, *J. Open Source Software* **6** (2021) 2807.

[21] C. Caprini and D.G. Figueroa, *Cosmological Backgrounds of Gravitational Waves*, *Class. Quant. Grav.* **35** (2018) 163001 [1801.04268].